

RECENT PROGRESSES IN THE PHYSICS OF SMALL-SCALE MAGNETIC FIELDS

Oskar Steiner

Kiepenheuer-Institut für Sonnenphysik, Schöneckstrasse 6, 79104 Freiburg, Germany, steiner@kis.uni-freiburg.de

ABSTRACT

New high-resolution observations reveal that small-scale magnetic flux concentrations have a delicate substructure on a spatial scale of $0.1''$. It can be basically interpreted in terms of a magnetic flux sheet or tube that vertically extends through the ambient weak-field or field-free atmosphere with which it is in mechanical equilibrium. A more refined interpretation comes from new three-dimensional magnetohydrodynamic simulations that are capable of reproducing the corrugated shape of magnetic flux concentrations and their signature in the visible continuum. Furthermore it is shown that the characteristic asymmetric shape of the contrast profile of facular granules is an effect of radiative transfer across the rarefied atmosphere of the magnetic flux concentration. Three-dimensional radiation magnetohydrodynamic simulation of the integral layers from the top of the convection zone to the mid-chromosphere show a highly dynamic chromospheric magnetic field, marked by rapidly moving filaments of stronger than average magnetic field that form in the compression zone downstream and along propagating shock fronts. The simulations confirm the picture of flux concentrations that strongly expand through the photosphere into a more homogeneous, space filling chromospheric field.

Key words: Sun; photosphere; chromosphere; magnetohydrodynamics.

1. INTRODUCTION

This paper focuses on small-scale magnetic flux concentrations in the photosphere and on aspects of the chromospheric magnetic field. Here, the term small-scale flux concentration is used to designate the magnetic field that appears in the form of a bright structure in G-band filtergrams consisting of tiny objects that can be found within and at vortices of intergranular lanes. They are also visible in the continuum, where single bright elements are called *facular points* (Mehlretter 1974) and the structure made up of bright elements the *filigree* (Dunn & Zirker 1973). In more recent times,

the small-scale magnetic field was mostly observed in the G-band because the molecular band-head of CH that constitutes the G-band acts as a leverage for the intensity contrast. Being located in the blue part of the visible spectrum, this choice also helps improving the spatial resolution that goes proportional with the wavelength. Small-scale magnetic flux concentrations are studied for several reasons:

- Small-scale magnetic flux concentrations are at the small end of a hierarchy of magnetic structures on the solar surface so that the question arises whether they are “elemental” or whether there are yet smaller flux elements. Why do they form? Are they a surface phenomenon? What is their origin?
- Small-scale magnetic flux concentrations near the solar limb are identified with faculae. Faculae on the other hand do critically contribute to the solar irradiance variation.
- Small-scale magnetic flux concentrations play probably a vital role in the transport of mechanical energy to the outer atmosphere, e.g., by photospheric “foot-point motion” with the subsequent formation of current sheets. They also guide and convert magnetoacoustic waves generated by the action of convective motion.

2. NEW OBSERVATIONS

Novel observations of unprecedented spatial resolution come these days from the recently commissioned 1 m Swedish Solar Telescope. Example snapshots of filtergrams in the G-band and in the H line of Ca II, supplemented with magnetograms, are discussed in detail by Berger et al. (2004) and Rouppe van der Voort et al. (2005). Fig. 1 shows an example out of the former paper, chosen to demonstrate that the “strings” and “crinkles” known from earlier images are revealed to be delicately corrugated ribbons that show structure on a scale of $0.1''$. This structure evolves on a shorter than granular time-scale, giving the impression of a separate (magnetic) fluid that resists mixing with the granular material. In this active region Fig. 1 belongs to, intergranular lanes are often completely filled with magnetic field like in the case

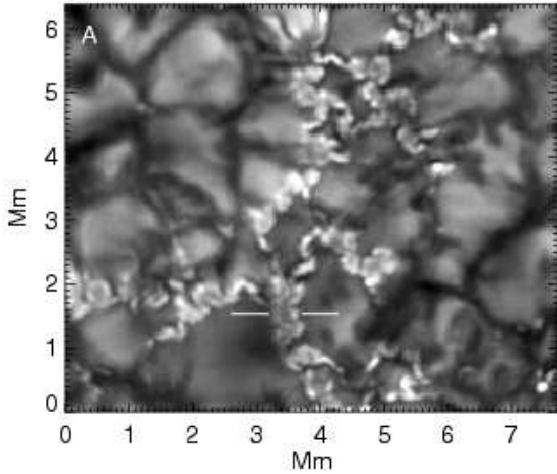


Figure 1. G-band filtergram showing the ribbon-like structure of magnetic flux concentrations. From Berger et al. (2004).

marked by the white horizontal lines in Fig. 1. There, and in other similar cases, the magnetic field concentration is framed by a striation of bright material, while the central part is dark.

This situation reminds of the flux-sheet model and the “bright wall effect”. The basic properties of this model are sketched in Fig. 2. Accordingly, a small-scale flux concentration, either of tube or sheet-like shape, is in mechanical equilibrium with the ambient atmosphere, viz., the gas plus magnetic pressure of the atmosphere in the tube/sheet equals the gas pressure in the ambient medium

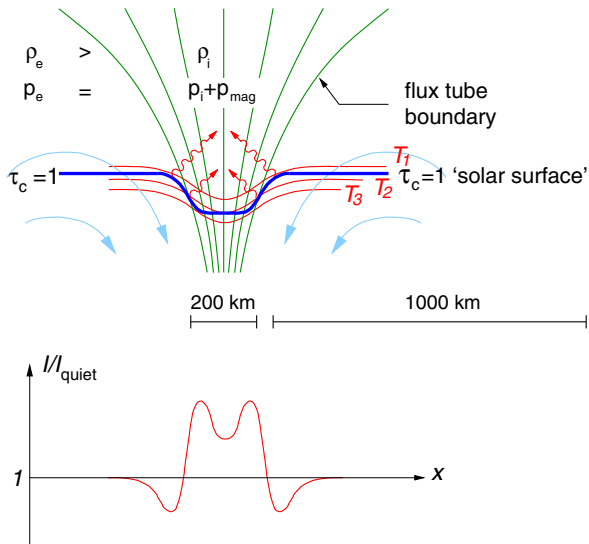


Figure 2. Sketch of a magnetic flux sheet (top) with corresponding intensity contrast (bottom). Note that the isothermal surfaces are not exactly parallel to the surface of optical depth unity, which gives rise to the particular M-shape of the contrast profile.

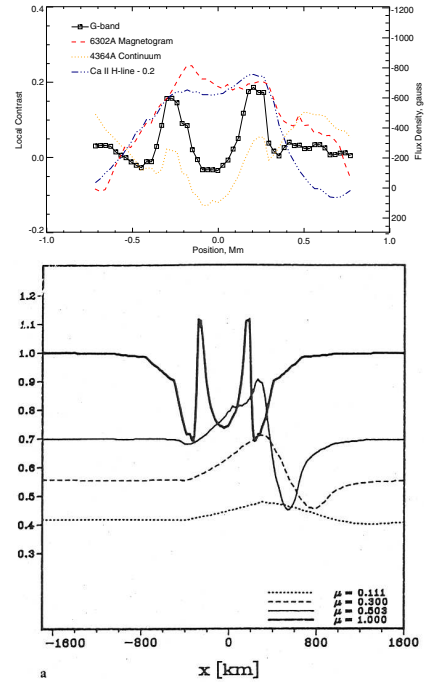


Figure 3. Top: G-band intensity (solid curve) along a section similar to but broader than the one indicated in Fig. 1. Also shown are the magnetogram signal, the continuum intensity at 436.4 nm and the Ca II H-line intensity down-shifted by 0.2. From Berger et al. (2004). Bottom: Continuum intensity at 500 nm from a medium sized “KGB” flux-sheet model for different heliocentric angles $\mu = \cos \theta$. From Knölker & Schüssler (1988).

at equal geometrical height. This can only be the case if the density in the flux concentration is reduced with respect to the environment, at least in the photospheric part, where the radiative heat exchange quickly drives the configuration towards radiative equilibrium, hence to a similar temperature at constant geometrical height. This density reduction renders the flux tube/sheet atmosphere more transparent, which causes a depression of the surface of constant optical depth, as indicated by the surface of $\tau_c = 1$ in Fig. 2. In a plage or network region, this effect increases the “roughness” of the solar surface, hence the effective surface from which radiation can escape, which increases the net radiative loss from these areas. Radiative cooling from the depression walls of the magnetic flux concentrations leads to a horizontal pressure gradient, which drives a plasma flow directed towards the flux tube/sheet.

A first quasi-stationary, quite self-consistent simulation of such a small-scale flux concentration was carried out by Deinzer et al. (1984a) and Deinzer et al. (1984b), popularly known as the “KGB-models”. Fig. 3 (bottom) shows the relative intensity emerging from one of these models (Knölker & Schüssler 1988). It corresponds to the plot in the bottom part of Fig. 2, which shows the intensity of light propagating in the vertical direction as a function of distance from the flux-sheet axis. The top panel of

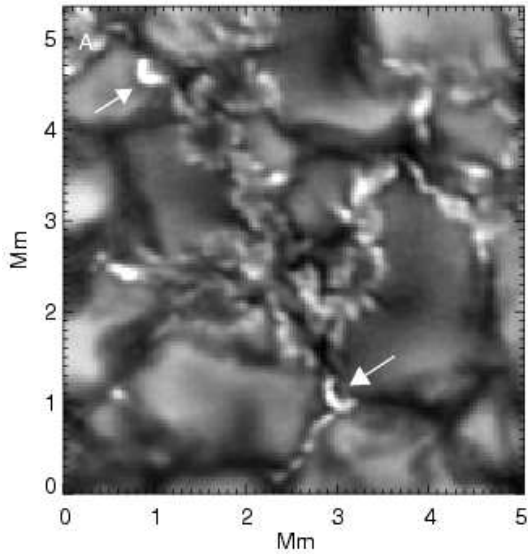


Figure 4. G-band filtergram showing a “flower structure” and two tiny “loop-like” features. From Berger et al. (2004).

Fig. 3 shows the emergent intensity from a cross section of a ribbon structure similar but about twice as wide as the one marked in Fig. 1 by the white horizontal lines. The similarity between the model (solid curve for heliocentric angle $\mu = 1$) and the observation ($\mu = 0.99$) is remarkable, although not exact. Also it must be noted that the model has a mean spatial resolution of about 20 km, four times better than the observation. Turning to a narrower flux sheet would result in a merging of the two contrast peaks into a single central peak in both, model and observation. Yet, the striation of the depression wall that can be seen in the observation is of course not reproduced by the model, which is strictly two-dimensional with translational invariance in lane direction.

Accordingly, the basic properties of ribbon-like magnetic flux concentrations can be understood in terms of a magnetic flux sheet embedded in and in force balance with a more or less field-free ambient medium. This is also true (replacing the word sheet by tube) for the rosette structure visible in the upper left region, centred at $(x, y) = (1.6, 3.9)$ Mm, of Fig. 4. This figure too is from the paper of Berger et al. (2004) who call this structure “flower-like”. Flowers can transmute to pores and vice versa. The striation of their bright collar is similar to that seen in ribbon structures. Discarding the striation, the basic properties of flowers can well be interpreted in terms of a tube shaped flux concentration as sketched in Fig. 2.

A puzzling and not uncommon feature are the “crinkles” indicated by arrows in Fig. 4. Continuing the line of reasoning from above, one could argue that these must be tube-like flux concentrations that are inclined so that only a crescent of the bright depression wall is visible. If so, one would still expect a more or less circular patch of po-

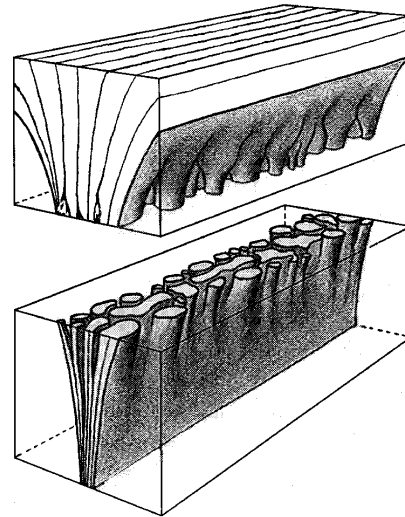


Figure 5. Sketch of filament formation due to the flute instability close to the surface of optical depth unity. From Bünte (1993).

larization signal, which however is not the case. Instead, the magnetogram signal (not shown here) closely follows the bright pattern, which rather suggests that a tiny photospheric loop was present, except that the two foot-points have the same polarity.

A 2 h sequence of images with a quality comparable to Figs. 1 and 4 (Roupe van der Voort et al. 2005) reveals that the shape of the ribbon-like flux concentrations and the striation of ribbons and flowers change on a very short time-scale, of the order of the Alfvén crossing travel time. This suggests that these morphological changes and the striation itself are related to the flute instability, which small-scale flux concentrations are liable to. For an untwisted axisymmetric flux tube, the radial component of the magnetic field at the flux-tube surface must decrease with height, $dB_r/dz|_S < 0$, in order that the flux tube is stable against the flute (interchange) instability (Meyer et al. 1977). While this condition is fulfilled for sunspots and pores with a magnetic flux in excess of $\Phi \approx 10^{19}$ Mx, small-scale flux concentrations do not fulfill it (Schüssler 1984; Steiner 1990; Bünte et al. 1993). Bünte (1993) shows that small-scale flux sheets too are flute unstable, and he concludes that filament formation due to the flute instability close to the surface of optical depth unity would ensue. The scenario is sketched in Fig. 5. However, as the flux sheet is bound to fall apart because of the flute instability, its debris are reassembled by the continuous advection back to the intergranular lane so that a competition between the two effects is expected to take place, which might be at the origin of the corrugation of the field concentrations and of the striation of the tube/sheet interface with the ambient medium.

Although the fine structure of small-scale magnetic flux concentrations changes on a very short time scale, single flux elements seem to persist over the full duration

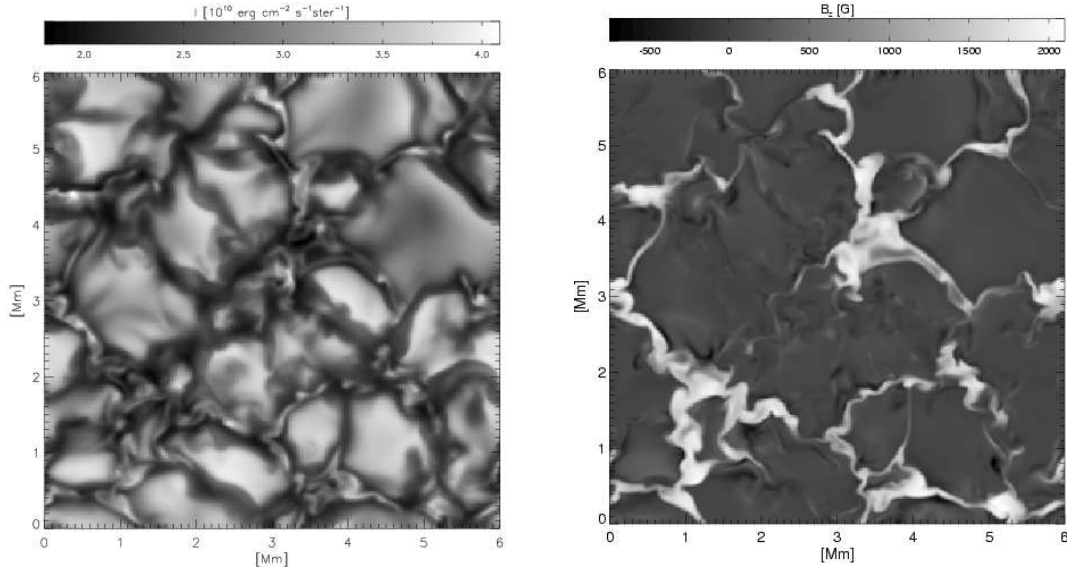


Figure 6. Simulation snapshot. Left: Frequency integrated intensity. Right: Vertical magnetic flux density at constant average geometrical height of optical depth unity. The mean flux density is 200 G. From Vögler et al. (2005).

of the time sequence of 2 h. They may dissolve or disappear for a short period of time, but it seems that the same magnetic flux reassembles to make them reappear nearby. This suggests a deep anchoring of at least some of these flux elements.

3. NEW SIMULATIONS

New results from simulations on the formation, dynamics and structure of small-scale magnetic flux concentrations have recently been published in a series of papers originating from the Max-Planck-Institut für Sonnensystemforschung. Vögler et al. (2005) simulate magnetoconvection in a box encompassing an area on the solar surface of 6×6 Mm with a height extension of 1400 km, reaching from the temperature minimum to 800 km below the surface of optical depth unity. Although this is only 0.4% of the convection zone depth, the box nevertheless includes the entire transition from almost complete convective to mainly radiative energy transfer and the transition from the regime where the flux concentration is dominated by the convective plasma flow to layers where the magnetic energy density of the flux concentrations by far surpasses the thermal energy density. The bottom boundary in this and similar simulations is open in the sense that plasma can freely flow in and out of the computational domain, subject to the condition of mass conservation. Inflowing material has a given specific entropy that determines the effective temperature of the radiation leaving the domain at the top, while the outflowing material carries the entropy it instantly has.

Fig. 6 shows a snapshot from this simulation: To the left the emergent mean intensity, to the right the vertical magnetic field strength at the horizontally averaged geomet-

rical height of optical depth unity. Clearly, the magnetic field shows a corresponding signal in the emergent intensity very much like the snapshots discussed in Sect. 2. Also the intensity signal shows the same corrugated and knotted ribbon structure that is observed, and sometimes there appear also broader ribbon structures with a dark central core. In the latter case however, the characteristic striation is absent, possibly because the flute instability is suppressed on very small spatial scales due to lack of sufficient resolution of the simulation. In the central part of the snapshot, a micro pore or magnetic knot has formed.

A comparison of the average gas plus magnetic pressure as a function of height at locations of magnetic flux concentrations with the run of the average gas pressure in weak-field regions reveals that even in this dynamic regime, the thin flux tube approximation is very well satisfied. This result confirms that the model of a quasi-static, thin flux tube in mechanical equilibrium with the ambient medium, as discussed in Sect. 2, is indeed an acceptable first approximation to the real situation.

Simulations are not just carried out for the sake of reproducing observed quantities. Once good agreement with all kind of observations exists, simulations allow with some confidence to inform about regions not directly accessible to observations. For example about the magnetic structure in subsurface layers. In this respect the simulations of Vögler et al. (2005) show that often flux concentrations that have formed at the surface disperse again in shallow depths, an observation that Schaffenberger et al. (2005) have equally made in their simulation with an entirely different code. A vertical section through a three-dimensional simulation domain of the latter work, where two such shallow flux concentrations have formed, is shown in Fig. 11. The superficial nature of magnetic flux concentrations in the simulations, however, is diffi-

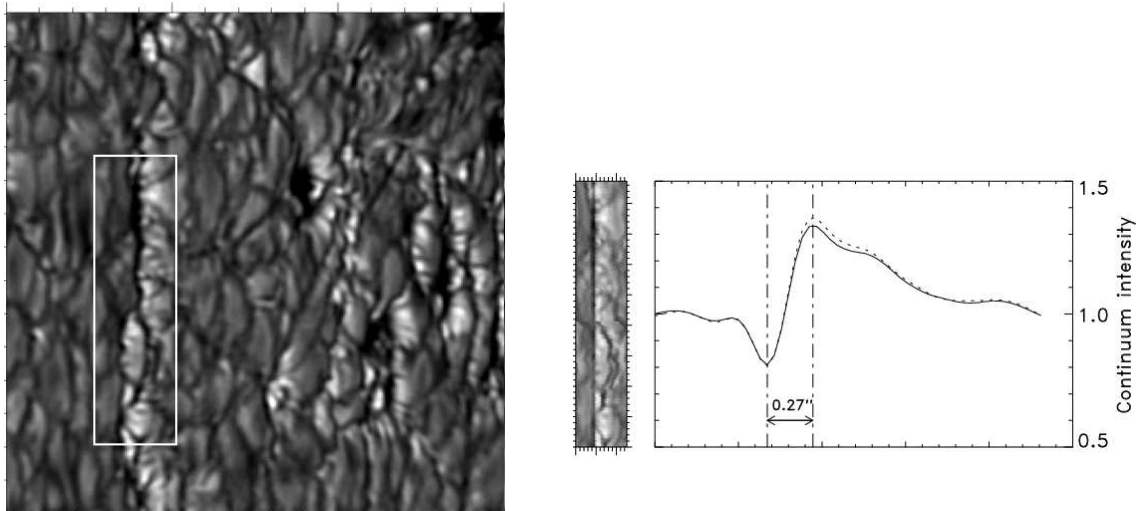


Figure 7. Left: Network faculae at a heliocentric angle of $\mu = 0.48$ in the continuum at 587.5 nm. The solar limb is to the right. Right: Faculae within the white box of the image to the left aligned according to the position of the dark lane, together with the mean spatial scan through the aligned faculae. From Hirzberger & Wiehr (2005).

cult to reconcile with the observation that many flux elements seem to persist over a long time period.

Simulation results usually have a better spatial resolution than is achievable with observations, which allows for predictions about observable quantities at higher than presently obtainable resolution. Using a snapshot like the one shown in Fig. 6, Khomenko et al. (2005b) compute emerging Stokes- V profiles, which they classify according to their shape and wavelength shift, etc. If degrading the spatial resolution of the snapshot to $0.5''$ by application of an instrumental point spread function, they find a patchwork of Stokes- V classes that does not correlate at all with the corresponding patchwork at full spatial resolution. This result discouragingly suggests that $0.5''$, which presently is an excellent angular resolution for spectro-polarimetric observations, is by an order of magnitude short of reliably informing about the magnetic structure of small-scale flux concentrations.

In another application, Khomenko et al. (2005a) derive histograms of synthesized Stokes- V amplitudes of Fe I 1.5648 μm and Fe I 630.2 nm from simulation snapshots with an average flux density of 10, 20, and 30 G and compare them to corresponding histograms of observed Stokes- V profiles. From this comparison they conclude that the average flux density of a quiet Sun internetwork region must be 20 G, 40 G less than is derived from Hanle-effect measurements by Trujillo Bueno et al. (2004).

4. THE PHYSICS OF FACULAE

With decreasing distance from the limb of the solar disk, small-scale magnetic flux concentrations increase in contrast against the quiet Sun background and appear as solar

faculae. Ensembles of faculae in the form of plage and network regions are a conspicuous feature of the white light solar disk, almost as conspicuous as sunspots. It is therefore not surprising that they play a key role in the solar radiance variation over a solar cycle and on shorter time scales (Fligge et al. 2000; Wenzler et al. 2005). There exists a long list of publications on center to limb measurements of the continuum contrast of faculae. Results are diverse however, as the contrast is not only a function of the heliocentric angle, $\mu = \cos \theta$, but also of facular size, magnetic field strength, spatial resolution, etc., and as measurements are prone to selection effects. While many earlier measurements report a contrast maximum around $\mu \approx 0.2 \dots 0.4$ with a decline towards the limb, latest measurements (Sütterlin et al. 1999; Ahern & Chapman 2000; Adjabshirizadeh & Koutchmy 2002; Ortiz et al. 2002; Centrone & Ermolli 2003; Vogler et al. 2004) point rather to a monotonically increasing or at most mildly decreasing contrast up to the limb.

The standard facula model (Spruit 1976), again consists of a magnetic flux concentration embedded in and in mechanical equilibrium with a weak-field or field-free environment as is sketched in Fig. 2. When approaching the limb, the limb side of the bright depression wall becomes ever more visible and ever more perpendicular to the line of sight, which increases its brightness compared to the limb darkened environment. At the extreme limb, obscuration by the centerward rim of the depression starts to take place, which decreases the size and possibly the contrast of the visible limb-side wall.

Recently, Lites et al. (2004) and Hirzberger & Wiehr (2005) have obtained excellent images of faculae with the 1 m Swedish Solar Telescope. Fig. 7 from Hirzberger & Wiehr (2005) shows on the left hand side network faculae at a heliocentric angle of $\mu = 0.48$ in the continuum at 587.5 nm. The solar limb is located towards the

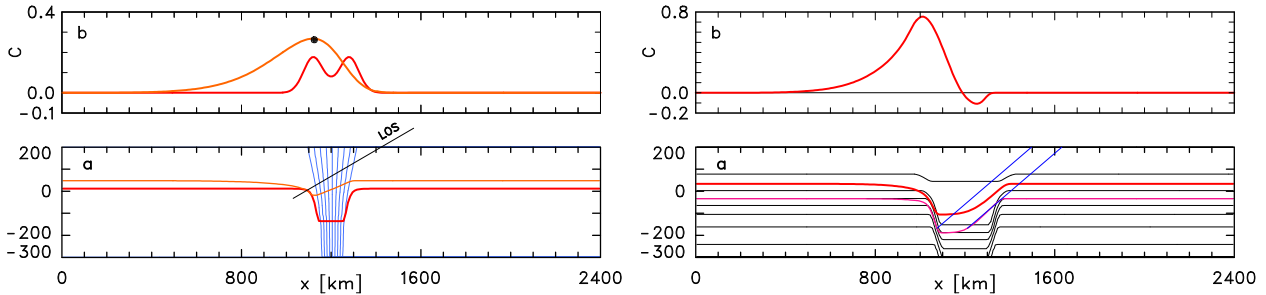


Figure 8. Left: a) Magnetic flux concentration (blue) with surfaces of optical depth $\tau = 1$ for vertical lines of sight (red curve) and lines of sight inclined by $\theta = 60^\circ$ to the vertical direction (light red curve). b) Corresponding contrast curves. All values of the light red curve left of the black dot originate from lines of sight left of the one indicated in panel a). Right: a) Surfaces of optical depth $\tau = 1$ and 5 (red) for lines of sight inclined by 50° to the vertical, together with isotherms. b) Contrast profile. The region of negative contrast is bounded by the two lines of sight (blue) indicated in panel a).

right hand side. It is clearly visible from this image that faculae are in reality partially brightened granules with a dark facular lane on the disk-center side of the contrast enhancement, which is also the location of the magnetic flux concentration. The right half of Fig. 7 shows the string of faculae within the white box of the image to the left, aligned according to the position of the dark lane. Also shown is the mean contrast profile, averaged over the alignment. Similar contrast profiles of single faculae are shown by Lites et al. (2004). Such contrast profiles pose now a new constraint that any model of faculae must satisfy.

Magnetoconvective simulations as the one discussed in Sect. 3 indeed show facular-like contrast enhancements when computing the emergent intensity along lines of sight that are inclined to the vertical direction for a synthesized limb observation. Such tilted simulation boxes are shown in two recent papers by Keller et al. (2004) and Carlsson et al. (2004). Keller et al. (2004) also show the contrast profile of two isolated “faculae”, which however have a more symmetric shape, rather than the characteristic steep increase on the disk-center side with the gentle decrease towards the limb. Also they obtain a maximum contrast of 2, far exceeding the observed value of about 1.3. It is not clear what the reason for this discrepancy might be. Interestingly, the “KGB-model” of Fig. 3 (bottom) does reproduce the asymmetric shape and the dark lane for heliocentric angles $\mu = 0.6$ and 0.3 .

In an attempt to better understand basic properties of faculae, Steiner (2005) considers a magnetohydrostatic flux sheet embedded in a plane parallel standard solar atmosphere. The flux-tube atmosphere is taken to be identical to the atmosphere of the ambient medium but it is shifted in the downward direction by the amount of the “Wilson depression” (the depression of the surface of continuum optical depth unity at the location of the flux concentration). In the photospheric part of the flux concentration however, thermal equilibrium with the ambient medium is enforced. Denoting with index i the flux-sheet atmosphere and with e the ambient atmosphere and with W the depth of the “Wilson depression”, the run of temper-

ature with height is therefore given by

$$T_i(z) = \begin{cases} T_e(z + W) & \text{for } \tau_c \gg 1 \\ T_e(z) & \text{for } \tau_c \ll 1, \end{cases} \quad (1)$$

where τ_c is the optical depth in the visible continuum. The lower left panel of Fig. 8 shows this configuration together with two surfaces of optical depth unity for vertical lines of sight (disk center) and for lines of sight running from the top right to the bottom left under an angle of $\theta = 60^\circ$ to the vertical, like the one indicated in the figure. The upper left panel shows the corresponding continuum enhancement for disk center (double humped) and $\theta = 60^\circ$. Of the curve belonging to $\theta = 60^\circ$, all values left of the black dot belong to lines of sight left of the one indicated in the lower panel. This means that the contrast enhancement extends far beyond the depression proper in the limbward direction, much like it is observed. The reason for this behaviour can be found in the radiative transfer effect explained in the following.

A material parcel located at the solar surface and lateral to the flux sheet “sees” a more transparent sky in the direction toward the flux sheet compared to a direction under equal zenith angle but pointing away from it because of the rarefied flux-sheet atmosphere. Correspondingly, from a wide area surrounding the magnetic flux sheet or flux tube, radiation escapes more easily in the direction towards the flux sheet so that a single flux sheet/tube impacts the radiative escape in a cross-sectional area that is much wider than the magnetic field concentration proper.

The right hand side of Fig. 8 shows a similar situation as to the left but for a flux sheet that is twice as wide. The continuum contrast for lines of sight inclined by $\theta = 50^\circ$ to the vertical is shown in the top panel. It can be seen that a dark lane of negative contrast enhancement occurs on the disk-center side of the facula. It arises from the low temperature gradient of the flux-sheet atmosphere in the height range of $\tau_c = 1$ and its downshift relative to the external atmosphere in combination with the inclined lines of sight. One could say that the dark lane in this case is an expression of the cool “bottom” of the magnetic flux sheet.

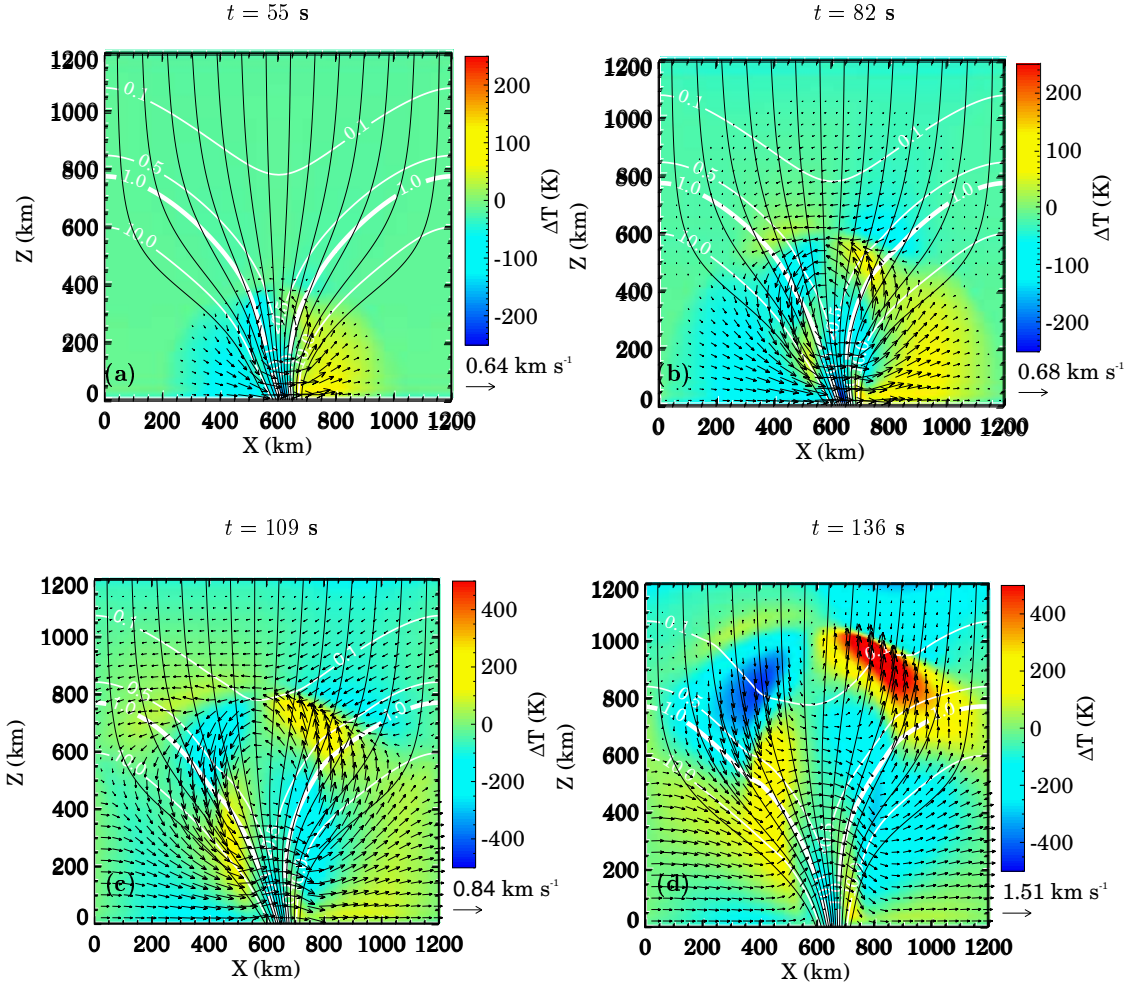


Figure 9. Flow pattern and temperature perturbation at four consecutive times in a magnetic flux concentration. They originate from an impulsive horizontal motion at the lower boundary, with an amplitude of 750 m/s, applied for half a wave period ($P = 240$ s), after which the motion ceases. The white curves denote contours of constant β corresponding to $\beta = 0.1, 0.5, 1.0$ (thick curve), and 10. From Hasan et al. (2005).

It is remarkable that this basic, energetically not self-consistent model is capable of producing both, the facular dark lane and the asymmetric contrast shape of the facula, with realistic contrast values. The results of this basic hydrostatic model carry over to a fully self-consistent model of a magnetic flux sheet in dynamic interaction with non-stationary convective motion (Steiner 2005). In this case the facular lane becomes broader and darker.

5. WAVES IN AND AROUND MAGNETIC FLUX CONCENTRATIONS

Progress in the understanding of wave propagation in and around magnetic flux concentrations come from recent simulations of two-dimensional waves in a stratified, magnetic medium, presented in two comprehensive papers by Rosenthal et al. (2002) and Bogdan et al. (2003). They emphasize the role of the surface of equal magnetic and thermal energy density, $p/e_{\text{mag}} = \beta = 1$ that acts

as a zone of wave mode conversion and wave deflection. As an illustrative example, Rosenthal et al. (2002) show a fast magnetoacoustic wave train that submits total internal reflection at the surface of $\beta = 1$ (the “canopy”), where the latter is inclined with respect to the incident wave front.

Small-scale magnetic flux concentrations do at the same time generate, convert, and deflect magnetoacoustic waves. As an example, Fig. 9 from Hasan et al. (2005) shows the propagation of an initial disturbance that consists in an impulsive horizontal displacement of the flux-sheet foot-point over a time period of 240 s with a maximal velocity of 750 m/s. The transverse motion of the flux sheet compresses the gas at the right interface of the sheet with the ambient medium, while in the wake of it on the left hand side, a pressure reduction occurs. The ensuing high-low pressure system generates a counterclockwise vortex motion that, as time proceeds, grows in size and moves upward. This upflow is guided along the field lines and leads to a longitudinal wave that steepens into a

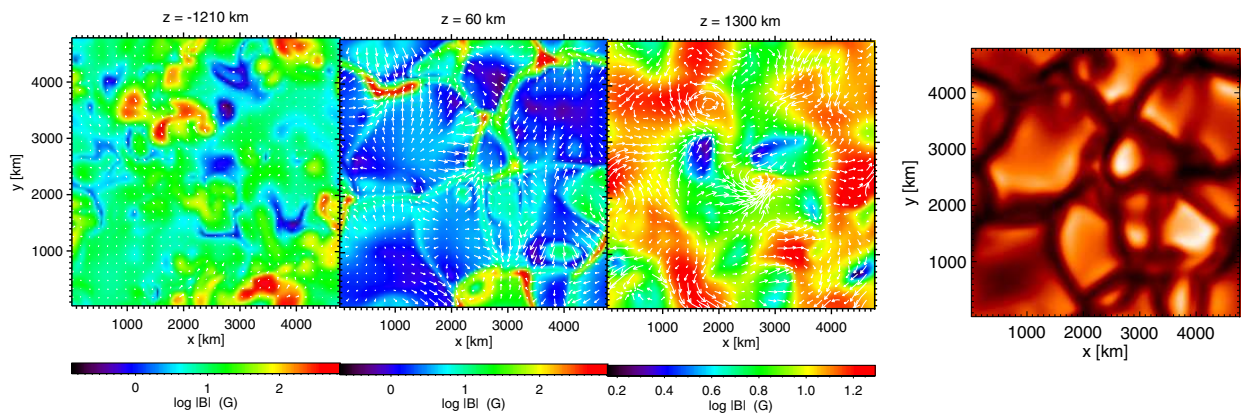


Figure 10. Horizontal sections through the three-dimensional computational domain. Color coding displays $\log |B|$ with individual scaling for each panel. Left: Bottom layer at a depth of 1210 km. Middle: Layer 60 km above optical depth $\tau_c = 1$. Right: Top, chromospheric layer in a height of 1300 km. White arrows indicate the horizontal velocity on a common scaling. Longest arrows in the panels from left to right correspond to 4.5, 8.8, and 25.2 km/s, respectively. Rightmost: Emergent visible continuum intensity. From Schaffenberger et al. (2005).

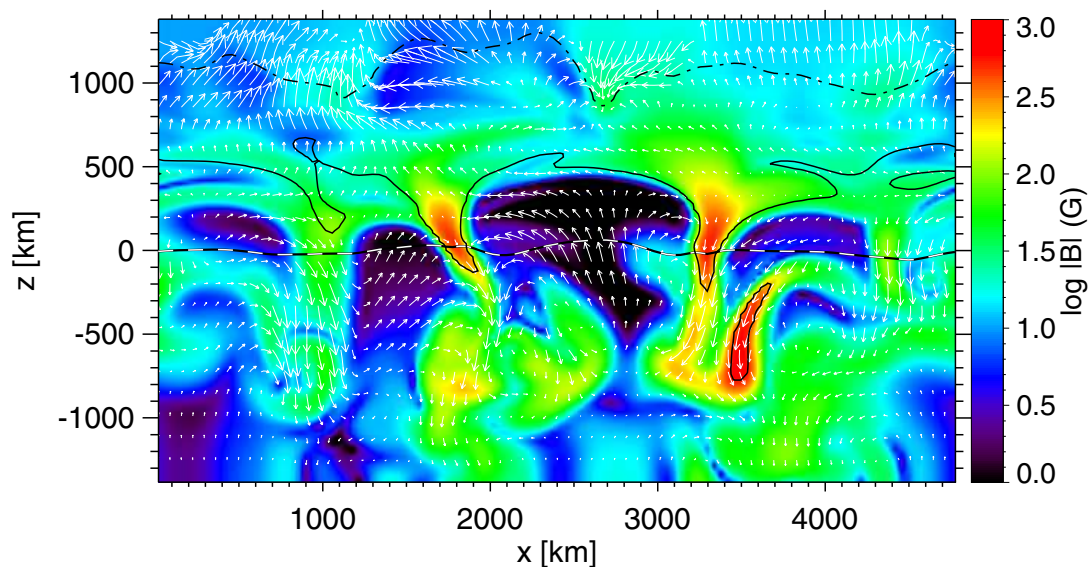


Figure 11. Snapshot of a vertical section through the three-dimensional computational domain, showing $\log |B|$ (color coded) and velocity vectors projected on the vertical plane (white arrows). The b/w dashed curve shows optical depth and the dot-dashed and solid black contours $\beta = 1$ and 100, respectively. From Schaffenberger et al. (2005).

shock at a height of about 900 km, along with a temperature enhancement of about 400 K.

Schaffnerberger et al. (2005) have developed a magneto-hydrodynamic code for studying wave propagation in a three-dimensional space that encompasses the integral layers from the top of the convection zone to the mid chromosphere. The code is based on a finite volume scheme, where fluxes are computed with an approximate Riemann-solver for automatic shock capturing. For the advection of the magnetic field components, a constrained transport scheme is used.

The three-dimensional computational domain extends from 1400 km below the surface of optical depth unity to 1400 km above it and it has a horizontal dimension of 4800×4800 km. The simulation starts with a homogeneous, vertical, unipolar magnetic field of a flux density of 10 G superposed on a previously computed, relaxed model of thermal convection. This low flux density is representative for magnetoconvection in a network-cell interior. The magnetic field is constrained to have vanishing horizontal components at the top and bottom boundary, but lines of force can freely move in the horizontal direction, allowing for flux concentrations to extend right to the boundaries. Because of the top boundary being located at mid-chromospheric height, the magnetic field is allowed to freely expand with height through the photospheric layers into the more or less homogeneous chromospheric field.

Fig. 10 shows the logarithm of the absolute magnetic flux density in three horizontal sections through the computational domain at a given time instant, together with the emergent Rosseland mean intensity. The magnetic field in the chromospheric part is marked by strong dynamics with a continuous rearrangement of magnetic flux on a time scale of less than 1 min, much shorter than in the photosphere or in the convection-zone layers. The field has a strength between 2 and 40 G in this snapshot, which is typical for the whole time series. Different from the surface magnetic field, it is more homogeneous and practically fills the entire space so that the magnetic filling factor in the top layers is close to unity. There seems to be no spatial correlation between chromospheric flux concentrations and the small-scale field concentrations in the photosphere.

Comparing the flux density of the panel corresponding to $z = 60$ km with the emergent intensity, one readily sees that the magnetic field is concentrated in intergranular lanes and at lane vertices. However, the field concentrations do not show a corresponding intensity signal like in Fig. 6. This is because the magnetic flux is too weak to form a significant “Wilson depression” (as can be seen from Fig. 11) so that no radiative channeling effect takes place.

Fig. 11 shows the logarithm of the absolute field strength through a vertical section of the computational domain. Overplotted are white arrows indicating the velocity field. The b/w dashed curve corresponds to the optical depth

unity for vertical lines of sight. Contours of the ratio of thermal to magnetic pressure, β , for $\beta = 1$ (dot-dashed) and $\beta = 100$ (solid) are also shown. Magnetoacoustic waves that form transient filaments of stronger than average magnetic field are a ubiquitous phenomenon in the chromosphere and are also present in the snapshot of Fig. 11, e.g., along the contour of $\beta = 1$ near $x = 1000$ km and $x = 2700$ km. They form in the compression zone downstream and along propagating shock fronts. These magnetic filaments that have a field strength rarely exceeding 40 G, rapidly move with the shock fronts and quickly form and dissolve with them.

The surface of $\beta = 1$ separates the region of highly dynamic magnetic fields around and above it from the more slowly evolving field of high beta plasma below it. This surface is located at approximately 1000 km but it is corrugated and its local height strongly varies in time.

6. CONCLUSIONS

Observations with the new 1 m Swedish Solar Telescope reveal that small-scale magnetic flux concentrations consists of a variety of elements, of which the most conspicuous are delicately corrugated, knotted ribbons whose fine structure evolves on a shorter than granular time scale. The basic properties of these elements can be interpreted in terms of magnetic flux sheets or tubes that vertically extend through the ambient weak-field or field-free atmosphere with which they are in mechanical equilibrium. The $0.1''$ substructure and its short time scale are possibly the result of the competing effect of flute instability and flux expulsion. For further progresses on the observational side, Stokes-vector polarimetry at an angular resolution $< 0.1''$ is needed to map the structure and dynamics of the magnetic field of small-scale flux concentrations.

Three-dimensional radiation magneto-hydrodynamic computer simulations are capable of reproducing many of the observed properties of small-scale flux concentrations, in particular its ribbon structure as seen in the continuum. Other details, like the characteristic striation of magnetic field interfaces or the asymmetric shape of the contrast profile of faculae cannot yet satisfactorily be reproduced. The latter can be traced to an effect of radiation transfer across magnetic flux concentrations. Nevertheless, the simulations warrant predictions about regions not directly accessible to observations. Accordingly, most small-scale flux concentrations seem to be not deeply rooted and they obey the thin flux-tube approximation rather well. A comparison of spectro-polarimetric data synthesized from simulation snapshots with observed data suggests a mean field strength in the internetwork of 20 G. Synthetic Stokes V maps also suggest that a spatial resolution of $< 0.1''$ is needed for spectro-polarimetric observations to reliably inform about the magnetic structure of small-scale flux concentrations.

For further progress with the simulations, boundary conditions for the magnetic field need to be relaxed so that for example magnetic field can be “pumped” across the bottom boundary and that the Poynting-flux can be determined at the top boundary. Simulation runs with diverse boundary conditions should develop a good intuition on the influence of boundary conditions on the formation, structure and dynamics of small-scale magnetic fields. Further progress is expected from higher spatial resolution and the application of modern high-resolution schemes. Extension of the simulation domain in all three spatial dimension will allow for a more realistic simulation of network fields and the coupling to the chromospheric magnetic field.

First 3-D radiation magnetohydrodynamic simulations that encompass a height range from the top layers of the convection zone to the mid-chromosphere give a first glimpse on the nature of the magnetoacoustic coupling between the photospheric and chromospheric regimes. They show a highly dynamic chromospheric magnetic field, marked by rapidly moving filaments of stronger than average magnetic field that form in the compression zone downstream and along propagating shock fronts. The surface of equipartition between magnetic and thermal energy density separates two different regimes of wave propagation above and below it. MHD-simulations of the integral layers from the convection zone to the chromosphere and the corona can be expected to substantially contribute to our understanding of these layers and their interaction with each other in the near future.

REFERENCES

- Adjabshirizadeh, A. & Koutchmy, S. 2002, in ESA SP-506: Solar Variability: From Core to Outer Frontiers, 415–418
- Ahern, S. & Chapman, G. A. 2000, *Sol. Phys.*, 191, 71
- Berger, T. E., Rouppe van der Voort, L. H. M., Löfdahl, M. G., et al. 2004, *A&A*, 428, 613
- Bogdan, T. J., Carlsson, M., Hansteen, V. H., et al. 2003, *ApJ*, 599, 626
- Büntje, M. 1993, *A&A*, 276, 236
- Büntje, M., Steiner, O., & Pizzo, V. J. 1993, *A&A*, 268, 299
- Carlsson, M., Stein, R. F., Nordlund, Å., & Scharmer, G. B. 2004, *ApJ*, 610, L137
- Centrone, M. & Ermolli, I. 2003, *Memorie della Società Astronomica Italiana*, 74, 671
- Deinzer, W., Hensler, G., Schüssler, M., & Weisshaar, E. 1984a, *A&A*, 139, 426
- Deinzer, W., Hensler, G., Schüssler, M., & Weisshaar, E. 1984b, *A&A*, 139, 435
- Dunn, R. B. & Zirker, J. B. 1973, *Sol. Phys.*, 33, 281
- Fligge, M., Solanki, S. K., & Unruh, Y. C. 2000, *A&A*, 353, 380
- Hasan, S. S., Van Ballegooijen, A. A., Kalkofen, W., & Steiner, O. 2005, *ApJ*, 631, 1270
- Hirzberger, J. & Wiehr, E. 2005, *A&A*, 438, 1059
- Keller, C. U., Schüssler, M., Vögler, A., & Zakharov, V. 2004, *ApJ*, 607, L59
- Khomenko, E. V., Martínez González, M. J., Collados, M., et al. 2005a, *A&A*, 436, L27
- Khomenko, E. V., Shelyag, S., Solanki, S. K., & Vögler, A. 2005b, *A&A*, in press
- Knölker, M. & Schüssler, M. 1988, *A&A*, 202, 275
- Lites, B. W., Scharmer, G. B., Berger, T. E., & Title, A. M. 2004, *Sol. Phys.*, 221, 65
- Mehltretter, J. P. 1974, *Sol. Phys.*, 38, 43
- Meyer, F., Schmidt, H. U., & Weiss, N. O. 1977, *MNRAS*, 179, 741
- Ortiz, A., Solanki, S. K., Domingo, V., Fligge, M., & Sanahuja, B. 2002, *A&A*, 388, 1036
- Rosenthal, C. S., Bogdan, T. J., Carlsson, M., et al. 2002, *ApJ*, 564, 508
- Rouppe van der Voort, L. H. M., Hansteen, V. H., Carlsson, M., et al. 2005, *A&A*, 435, 327
- Sütterlin, P., Wiehr, E., & Stellmacher, G. 1999, *Sol. Phys.*, 189, 57
- Schaffnerberger, W., Wedemeyer-Böhm, S., Steiner, O., & Freytag, B. 2005, in *Chromospheric and Coronal Magnetic Fields*, ESA Publication SP-596, 299–300
- Schüssler, M. 1984, *A&A*, 140, 453
- Spruit, H. C. 1976, *Sol. Phys.*, 50, 269
- Steiner, O. 1990, PhD thesis, ETH-Zürich, Nr. 9292
- Steiner, O. 2005, *A&A*, 430, 691
- Trujillo Bueno, J., Shchukina, N., & Asensio Ramos, A. 2004, *Nature*, 430, 326
- Vögler, A., Shelyag, S., Schüssler, M., et al. 2005, *A&A*, 429, 335
- Vogler, F. L., Brandt, P. N., Otruba, W., & Hanselmeier, A. 2004, in *Solar Magnetic Phenomena*, ed. A. Hanselmeier, A. Veronig, & M. Messerotti, proceeding of the Kanzelhöhe summer school 2003 (Kluwer), in press
- Wenzler, T., Solanki, S. K., & Krivova, N. A. 2005, *A&A*, 432, 1057